

Two-site recognition of *Staphylococcus aureus* peptidoglycan by lysostaphin SH3b

Luz S. Gonzalez-Delgado  ^{1,2,5}, Hannah Walters-Morgan ^{3,5}, Bartłomiej Salamaga ^{1,2},
Angus J. Robertson ^{1,2}, Andrea M. Hounslow ^{1,2}, Elżbieta Jagielska ⁴, Izabela Sabała ⁴,
Mike P. Williamson  ^{1,2*}, Andrew L. Lovering  ^{3*} and Stéphane Mesnage  ^{1,2*}

Lysostaphin is a bacteriolytic enzyme targeting peptidoglycan, the essential component of the bacterial cell envelope. It displays a very potent and specific activity toward staphylococci, including methicillin-resistant *Staphylococcus aureus*. Lysostaphin causes rapid cell lysis and disrupts biofilms, and is therefore a therapeutic agent of choice to eradicate staphylococcal infections. The C-terminal SH3b domain of lysostaphin recognizes peptidoglycans containing a pentaglycine crossbridge and has been proposed to drive the preferential digestion of staphylococcal cell walls. Here we elucidate the molecular mechanism underpinning recognition of staphylococcal peptidoglycan by the lysostaphin SH3b domain. We show that the pentaglycine crossbridge and the peptide stem are recognized by two independent binding sites located on opposite sides of the SH3b domain, thereby inducing a clustering of SH3b domains. We propose that this unusual binding mechanism allows synergistic and structurally dynamic recognition of *S. aureus* peptidoglycan and underpins the potent bacteriolytic activity of this enzyme.

Lysostaphin is a bacteriolytic enzyme produced and secreted by *Staphylococcus simulans* biovar *staphylolyticus*¹. This exotoxin has a potent activity against a wide range of staphylococci including the opportunistic nosocomial pathogen *S. aureus*². It displays endopeptidase activity and cleaves the pentaglycine crossbridges present in peptidoglycan (PG), the essential component of the bacterial cell wall, leading to rapid cell lysis. In *S. simulans* biovar *staphylolyticus*, immunity to lysostaphin is conferred by Lif, an aminoacyl transferase that introduces serine residues into PG crossbridges³. This modification dramatically reduces susceptibility to lysostaphin.

Owing to its powerful antistaphylococcal activity against both planktonic cells and biofilms⁴, lysostaphin has been extensively studied as a therapeutic agent to treat infections caused by methicillin-resistant *Staphylococcus aureus* (MRSA)^{5–11}. Recent studies have reported the design of lysostaphin variants with a reduced antigenicity and enhanced therapeutic efficacy^{12,13} as well as strategies to harness the bactericidal activity of this toxin^{14–16}. Collectively, the studies published have demonstrated that lysostaphin represents a credible therapeutic agent to combat staphylococcal infections, either alone or in combination with antibiotics¹⁷.

Lysostaphin is a modular hydrolase produced as a preproenzyme. It comprises a signal peptide, 15 N-terminal repeats of 13 amino acids, a catalytic domain with glycolylglycyl endopeptidase activity and a C-terminal PG-binding domain of 92 residues³. The specificity of lysostaphin toward staphylococci has been attributed to its binding domain, which recognizes pentaglycine crossbridges^{18,19}. Recent crystallographic studies have confirmed early models and showed that the pentaglycine stem is recognized by a shallow groove formed between strands β 1– β 2 and the RT loop, the binding specificity being essentially conferred by steric hindrance²⁰. Despite this exquisite recognition mechanism, the SH3b domain displays a

very weak affinity for the pentaglycine stems and binding has been shown to be optimal with multimeric PG fragments, suggesting a mechanism more complex than initially anticipated^{20,21}.

Here we combine NMR and X-ray crystallography to elucidate the mechanism underpinning the recognition of staphylococcal PGs by the lysostaphin SH3b domain. We show that the SH3b domain contains two binding sites located on opposite sides of the protein, allowing a mutually exclusive recognition of these two PG moieties. The recognition of the pentaglycine crossbridge and the peptide stem is therefore shared by two independent SH3b domains, allowing protein clustering on the PG. We propose that the combination of low affinity and high off-rate binding results in a synergistic and structurally dynamic binding that is particularly suitable for the recognition of non-contiguous epitopes of mature physiological PG. This unusual mechanism underpins the potent activity of lysostaphin and its capacity to punch holes in the cell walls to cause rapid cell lysis.

Results

NMR analysis of SH3b–PG interactions. We sought to investigate the mechanism underpinning the SH3b–PG interaction using NMR titrations with a panel of ligands of increasing complexity. Six ligands were produced, either by solid-phase synthesis or purified from *S. aureus* PG after digestion by hydrolytic enzymes (Supplementary Fig. 1). The ligands tested corresponded to a tetrasaccharide (GlcNAc–MurNAc–GlcNAc–MurNAc; GMGM), a pentaglycine crossbridge (GGGGG; G5), a tetrapeptide stem (A γ QKA; P4), a tetrapeptide with the pentaglycine as a lateral chain (A γ QK[GGGGG]A; P4–G5), a disaccharide–peptide dimer (GlcNAc–MurNAc–A γ QK[GGGGG]AA–GlcNAc–MurNAc–A γ QK[GGGGG]A; (GM–P4–G5)₂) and the peptide A γ QK[GGGGG]AA–A γ QKA (P5–G5–P4), which contains two peptide stems crosslinked via a single pentaglycine crossbridge.

¹Department of Molecular Biology and Biotechnology, University of Sheffield, Sheffield, UK. ²Krebs Institute, University of Sheffield, Sheffield, UK.

³Institute of Microbiology and Infection, and School of Biosciences, University of Birmingham, Birmingham, UK. ⁴International Institute of Molecular and Cell Biology, Warsaw, Poland. ⁵These authors contributed equally: Luz S. Gonzalez-Delgado, Hannah Walters-Morgan. *e-mail: m.williamson@sheffield.ac.uk; a.lovering@bham.ac.uk; s.mesnage@sheffield.ac.uk

Complete resonance assignment of the doubly labeled SH3b domain was obtained using standard triple resonance experiments (Supplementary Fig. 2). The six ligands were used to measure chemical shift perturbations (CSPs) associated with main-chain and side-chain amides (Supplementary Fig. 3 and Supplementary Table 1).

In agreement with previous studies, our results showed that pentaglycine (G5) peptides interact with several residues located in a narrow cleft corresponding to the binding groove originally proposed for *Staphylococcus capitnis* ALE-1, a close homolog of lysostaphin. These included residues N405–Y411, T429, G430, M453, D456 and Y472 (Fig. 1a and Supplementary Fig. 3a). CSPs of the signals corresponding to SH3b residues following addition of this ligand indicated a fast exchange rate with a weak binding affinity in the millimolar range ($K_D = 890 \pm 160 \mu\text{M}$).

S. aureus PG is highly crosslinked and therefore contains mostly tetrapeptide stems (P4). The SH3b domain bound to P4 peptides with a fast exchange rate and a low affinity ($K_D = 963 \pm 198 \mu\text{M}$), suggesting that this minimal ligand (like the G5 peptide) is not the complete PG motif recognised by the SH3b domain. Surprisingly, residues presenting pronounced CSPs upon binding to the P4 ligand were located on the side of the protein opposite to the G5-binding cleft (for example, N421, I425, A443 and V440; Fig. 1b and Supplementary Fig. 3b). The side chain of R427 also showed a pronounced CSP. Two hydrophobic residues presenting relatively large CSPs were buried in the structure, suggesting that they were not directly in contact with the P4 ligand (V461 and L473). This observation implies that whereas binding at G5 is fairly rigid lock-and-key, binding at P4 is more of an induced fit interaction, with adaptation of the protein to fit its ligand.

As expected, a tighter binding was observed for two PG monomer ligands made of the tetrapeptide stem with a pentaglycine lateral chain alone (P4–G5; $K_D = 98 \pm 42 \mu\text{M}$). The most prominent CSPs corresponded to residues previously identified with the simple ligands G5 and P4 in both cases (Fig. 1b,c). Several residues broadened and disappeared with the P4–G5 ligand (N405, I425, V461, G462, Y472 and L473), indicating a slow-to-medium exchange rate (Supplementary Fig. 3c). Titrations with a synthetic tetrasaccharide (GlcNAc–MurNAc)₂ revealed no interactions between the protein and the synthetic disaccharides, suggesting that the sugars do not play a key role in the recognition of PG by the SH3b domain.

Next, we studied the binding of the SH3b domain to dimeric PG fragments made of two peptide stems crosslinked by a pentaglycine chain. One of these ligands contained a single pentaglycine chain (P5–G5–P4), whilst the other had two (GM–P5–G5–GM–P4–G5). The largest CSPs associated with binding were those previously identified with simpler ligands (G5 and P4; Fig. 1d,e and Supplementary Fig. 3d,e). The CSPs corresponding to the recognition of the P4/P5 or G5 moieties were typical of a fast exchange rate, with an affinity of $100 \pm 34 \mu\text{M}$ for the P5–G5–P4 ligand. In the case of the most complex ligand (GM–P5–G5–GM–P4–G5), we could not determine any binding affinity as the protein started to precipitate in the presence of four equivalents of ligand resulting in the disappearance of the signals. One surface residue (W489) located close to residues binding the peptide stem only displayed CSPs with dimeric ligands. Interestingly, the CSPs observed for the larger ligands had fewer large changes than were seen for the simpler ligands (Supplementary Fig. 3).

Collectively, NMR titrations suggested that the SH3b domain recognises both the PG peptide stems and crossbridges via distinct sets of residues located on opposite sides of the protein surface.

Structure of the complex between SH3b and *S. aureus* PG peptide stem. We attempted to co-crystallize the SH3b domain with a branched P4–G5 ligand and were successful in obtaining crystals that diffracted to a resolution of 1.4 Å. Our initial expectation was to observe this ligand binding to the surface of a single SH3b domain,

but upon solving the structure, it was apparent that the G5 was recognized by one domain and P4 by another (symmetry-related copy) as shown in Fig. 2. The high-resolution (1.4 Å) synchrotron set is able to trace three of the P4 units (γ QKA, representing units 2–4) and a lower-resolution (2.5 Å) home source set is essentially identical but allows tracing of the full P4 ligand (A γ QKA). In our structures, the pentaglycine bridge sits identically to that of other SH3b structures (PDB accession 5LEO), but then projects the crossbridge link (K to G5) and stem peptide (A γ QKA) into a pocket located on the opposite side of a second SH3b monomer (Fig. 2a–c). The two SH3 domains make no strong interactions with one another, but display a shape–surface complementarity that allows for close contact around the shared ligand.

The P4 and G5 components of the ligand are at approximately 90° angles to one another, and the carbon atoms of the K3 side chain make favorable contacts with the hydrophobic side chains of Y407, T422', I424' and W489' (prime is used to denote the opposing SH3b). Units one to three of the P4 PG stem display a linear β -like conformation, with peptide bonds hydrogen bonding to residues from both SH3b domains: γ Q2 NH to carbonyl of K406, K3 NH to carbonyl of D423' and K3 CO to NH of I425'. This arrangement makes for much stronger contacts between the SH3b domains and P3 or P4 as compared to P1 or P2, and would place the attached physiological PG saccharide units at the edge of both monomers. There is a clearly defined pocket for the terminal D-Ala4 (Fig. 2d), with the COO group making a salt-bridge to the side chain of R427', and a hydrophobic pocket comprising I424', I425', R433', H458', W460', P474' and W489' surrounding the methyl side chain of the substrate. Sequence and structure alignments between lysostaphin SH3b (SH3_5) and other proteins indicate that the P4 D-Ala–carboxylate pocket is likely a conserved feature of wider superfamily members (Supplementary Fig. 4), with relevance for both SH3_3 and SH3_4 subgroups. There are no current structures for the latter, but the two SH3_4 domains of *Clostridium* phage lysin phiSM101 each have a carboxylate ligand bound at this position, suggesting an important role for the residues equivalent to lysostaphin R427 (ref. 22).

Mutational analysis of the binding activity. We sought to confirm the contribution of the SH3b residues identified by NMR and X-ray crystallography to recognition of the crossbridge (G5) and peptide stem (P4) ligands. Six single-site substitution mutant domains were produced and analyzed by NMR (N405A, M453A, Y472S, I425A, R427M and W489L). ¹⁵N HSQC (heteronuclear single quantum coherence spectroscopy) spectra of all mutant domains revealed that these were properly folded, allowing us to measure CSP values in the presence of the maximum concentration of ligand previously used (32 equivalents). As expected, all mutations were associated with a reduction in CSPs as compared to the wild-type domain (Supplementary Fig. 5). We characterized the reduction in binding affinity using a figure of residual binding, which is defined as the mutant to wild type ratio of chemical shift changes, averaged over all amino acids. Given the weak binding affinities, and the fact that the protein concentration is always lower than the affinity, these correspond roughly to the expected reduction in affinity. Domains with substitutions in the residues involved in the interaction with G5 still retained a relatively high residual binding, the N405A substitution having the most pronounced effect (16% residual binding for the N405A mutant, 55.5% for M453A and 24.6% for Y472S). Whilst the I425 mutant still displayed 29.4% residual binding, the R427M and W489L substitutions had a major impact on binding to the P4 ligand (1.6% and 6.6% residual binding, respectively). These results confirmed the contribution of the residues identified by NMR and crystallography to the binding of minimal ligands. The limited impact of most of the substitutions studied on binding is in agreement with the X-ray and NMR results, which revealed that the recognition of PG fragments by SH3b domains relies on a complex network of interactions.

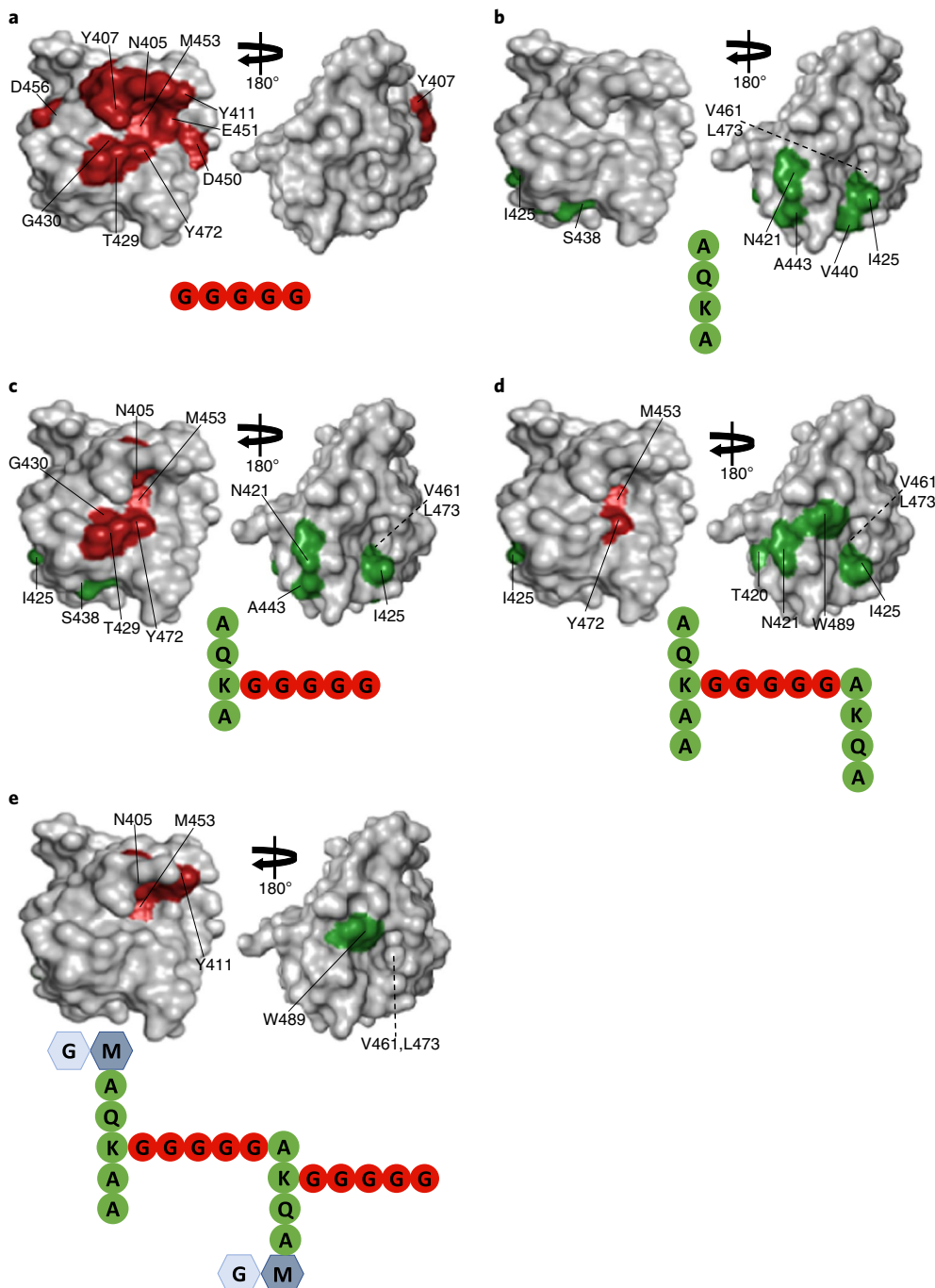


Fig. 1 | Mapping the interaction surface of the SH3b domain with synthetic *S. aureus* PG fragments. **a–f**, For each NMR titration, the average CSP was calculated and two-fold average CSP was chosen as a threshold to identify surface residues interacting with ligands. The residues interacting with the pentaglycine crossbridges are highlighted in red, those interacting with the peptide stem in green. Interaction maps corresponding to six ligands are shown. **a**, G5 peptide; **b**, P4; **c**, P4-G5; **d**, P5-G5-P4; **f**, GM-P5-G5-GM-P4-G5. Titrations confirmed the existence of a narrow cleft previously proposed to bind the PG crossbridges¹⁹ and recently shown to interact with pentaglycine²⁰. They also revealed a set of residues interacting with the peptide stem, located on the face of the protein opposite to the G5-binding cleft.

Binding of SH3b derivatives to purified PG sacculi. Owing to the labor-intensive nature of NMR analyses, and the fact that these analyses are limited to the study of interactions with soluble substrates, we designed a quantitative *in vitro* binding assay with PG sacculi, which represent the natural substrate of lysostaphin. The SH3b domain was fused to the monomeric fluorescent protein mNeonGreen²³ to follow binding in the presence of increasing amounts of PG (Fig. 3 and Supplementary Table 2). Recombinant proteins were

purified using two chromatography steps including metal affinity and gel filtration. As a first step we measured the binding of SH3b-mNeonGreen fusions to PG purified from the wild type and from *femB* and *femAB* mutants (containing five, three and one glycine residue in crossbridges, respectively; Fig. 3a and Supplementary Fig. 6). As expected, binding occurred in a dose-dependent manner and binding to the *femB* mutant was clearly reduced (1.71-fold change), whilst a more drastic reduction in binding was observed

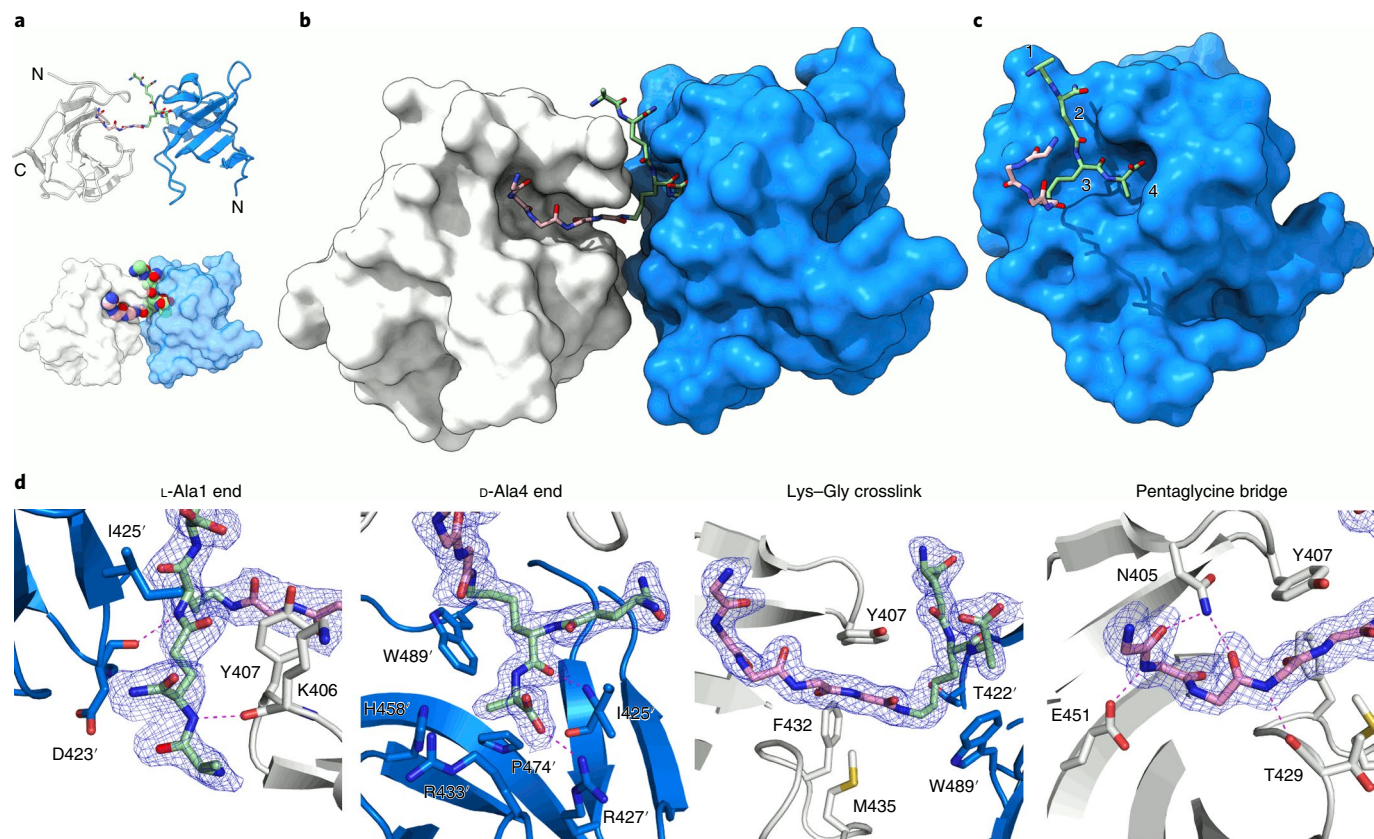


Fig. 2 | Structure of lysostaphin SH3b in complex with the P4-G5 ligand. The SH3b domain and a symmetry-related partner are colored white and blue, respectively, and the ligand is colored by atom type, with P4 C atoms in green and G5 C atoms in pink. **a**, Protein folds with termini labeled and two representations (fold and ligand in ribbon and stick formats, respectively, and surface format). **b**, Co-crystal structure showing the SH3b-ligand shape complementarity. **c**, Rotated view of a single SH3b domain showing the interaction with the P4 ligand (blue, with peptide units labeled 1–4). **d**, Experimental $2F_o - F_c$ difference map contoured at 1σ for different regions of the bound ligand, with selected interacting residues in stick form. The L-Ala1 end panel is from the 2.5-Å dataset, others are from the 1.4-Å dataset. Residues from the symmetry-related SH3b domain are denoted by use of a prime (') and hydrogen bonds are represented as a dashed line.

with the *femAB* mutant (2.20-fold change). The residual, dose-dependent binding to the *fem* mutant PGs is in agreement with our identification of a second site recognizing the peptide stems. Fifteen recombinant fusions with mutations in residues previously identified were purified and their binding activity was measured (Fig. 3b,c and Supplementary Fig. 6). Most of the mutations clearly impaired binding to PG to a level similar to the level of binding displayed by the wild-type SH3b-mNeonGreen fusion to the *femB* PG. The biggest impact on binding was observed for the R427M and W489L substitutions, which impaired the recognition of peptide stems (2.47- and 2.18-fold changes, respectively, as compared to the wild type). These results therefore confirmed the role of the residues identified by NMR and X-ray crystallography and provided the first evidence that peptide stem recognition by the lysostaphin SH3b domain is critical for binding.

Impact of SH3b mutations on lysostaphin activity. The SH3b mutations previously described (Supplementary Fig. 6) were introduced into the mature lysostaphin enzyme. Recombinant proteins were purified and serial twofold dilutions were spotted on agar plates containing autoclaved *S. aureus* cells as a substrate (Supplementary Fig. 7). The enzymatic activity was detected as a clearing zone resulting from the solubilization of *S. aureus* cell walls. Four independent series of protein purifications were carried out, each including a wild-type lysostaphin protein. One lysostaphin mutant (M453A), which showed an aberrant circular dichroism spectrum, could not be analyzed; mutant R427M was also excluded

from the study as it did not bind to the nickel column. Among all the substitutions tested, Y472S and W489L led to the most important effects observed (ninemfold decrease), whilst all the others had only a limited impact. These results were in line with the binding assays, indicating that no single mutation abolished enzymatic activity and supported our results indicating that the recognition of the peptide stem is equally, if not more, important for binding and activity as binding to the pentaglycine bridge.

Discussion

The crystal structure reported here shows that SH3b has two well-defined binding sites for *S. aureus* PG: a narrow groove that accommodates the G5 lateral chain, with a tightly defined geometry and thus little tolerance for amino acid variants; and a more open site for the P4 peptide stem. One might therefore expect that the specificity for *S. aureus* PG arises entirely from the G5 site, which should be critical for binding. This is not what is indicated by the other results reported here.

The interpretation of CSPs, and of the affinities determined by fitting CSPs to a saturation curve, is more complex than may at first appear. A perturbation of a ^{15}N or ^1H nuclear shielding is typically caused by a change in the chemical environment at the nucleus, for example, owing to a change in hydrogen bonding or a change in the position of neighboring functional groups. Hydrogen bonding is highly directional, implying that increased mobility of a ligand within its binding site will result in smaller CSPs. Increased mobility will not necessarily result in weaker overall binding, because the

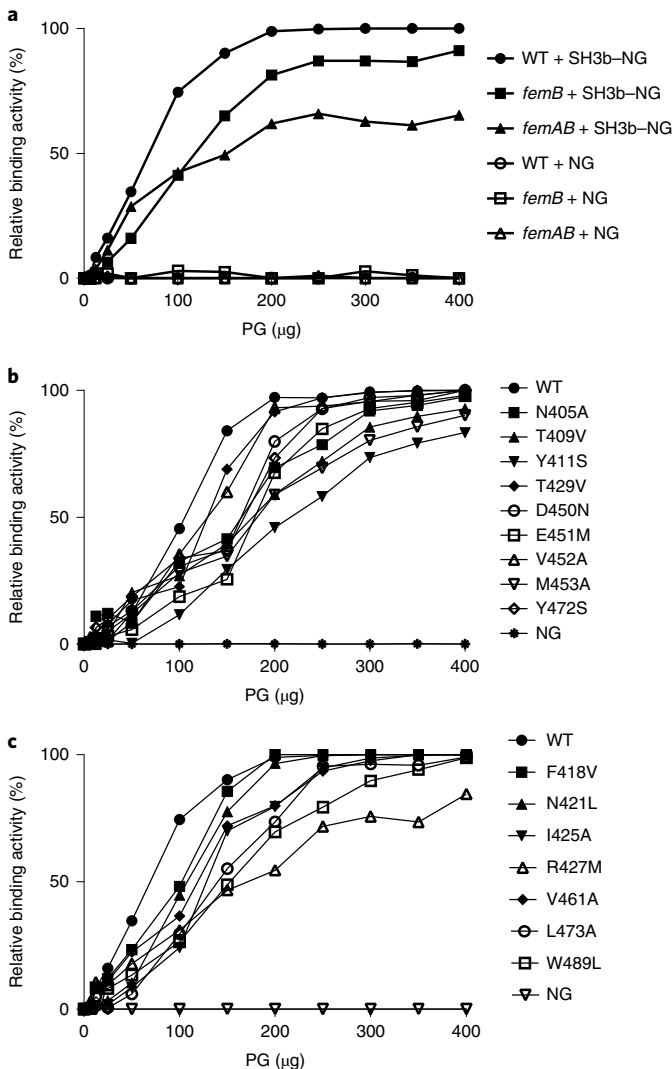


Fig. 3 | Binding activity of recombinant SH3b-mNeonGreen proteins to purified *S. aureus* PG. **a**, PG-binding activities of wild-type (WT) SH3b-mNeonGreen fusions (SH3b-NG) with wild-type *S. aureus* and *fem* mutants with altered PG crossbridges. **b**, PG-binding activities of wild-type SH3b-mNeonGreen and derivatives with substitution of residues involved in the interaction with the G5 ligand. **c**, PG-binding activities of wild-type SH3b-mNeonGreen and derivatives with substitution of residues involved in the interaction with the P4 ligand. The graphs show dose-binding responses whilst Supplementary Table 2 indicates the amount of PG required for 50% binding (PG_{50}) and the corresponding fold change as compared to the amount of PG required for 50% binding of the wild-type protein as a reference.

loss in enthalpy owing to a weaker time-averaged hydrogen bond can easily be compensated by a gain in entropy. Smaller CSPs can therefore indicate a more dynamic binding interaction, rather than just weaker binding. This phenomenon matches what is observed here (Supplementary Fig. 3). With a simple G5 or P4 ligand that binds in a single site, there are some large CSPs, clearly defining the location of the site (Supplementary Fig. 3a,b). With larger ligands, although the affinity is stronger (implying cooperative binding at both sites, see below), there are fewer large CSP values. The most obvious interpretation is that within each site the ligand has greater mobility, presumably because the physical linkage between the G5 and P4 groups prevents the larger ligands from binding optimally in both sites simultaneously.

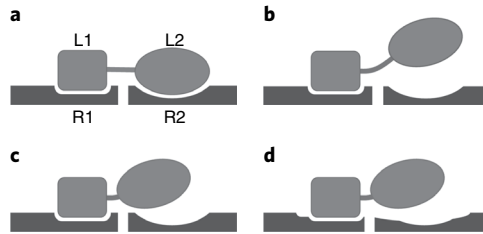


Fig. 4 | Models for binding of a ligand at two sites. **a**, Schematic of a receptor with two sites (R1 and R2), which bind the L1 and L2 ligand sites, respectively. L1 and L2 are connected by a flexible linker. **b**, The flexibility of the linker allows the R1 site to stay attached, but the R2 site to detach. The effective concentration of L2 at the R2 site (and thus the cooperativity of binding) will depend on the length and flexibility of the linker. **c**, If the linker is too short, it is not possible for the ligand to bind simultaneously at both R1 and R2. It can alternate between both sites, which will still result in cooperative binding, though less than in **b**. **d**, A weaker enthalpy of binding (for example, owing to the shortness of the linker preventing optimal binding at both sites) can to some extent be compensated by greater entropy (increased relative motion of ligand and receptor) if there is weak binding in non-optimal positions.

There have been many analyses published of binding affinities of ligands that interact via two different sites. A powerful approach is the concept of effective concentration^{24,25}. Consider a ligand L1–L2 that binds at two sites, R1 and R2, with a flexible linker between L1 and L2 (Fig. 4a). If the ligand detaches from site R2, then the rate at which L2 rebinds at R2 is given by $k_{on} \times [L2]_{eff}$, where k_{on} is the rate constant for binding and $[L2]_{eff}$ is the effective concentration of L2 at the R2 binding site (Fig. 4b). For a short linker with optimal length and geometry, $[L2]_{eff}$ can be orders of magnitude larger than $[L2]$, leading to much stronger binding than would be seen in the absence of L1 (because the overall affinity for L2 is equal to the off-rate divided by the on-rate and we can assume that the off-rate is unaffected by the presence of the linker). In other words, this can be described as cooperative binding, the affinity for the intact ligand L1–L2 being much stronger than the affinity for L1 or L2 alone. Conversely, if the linker is too short (Fig. 4c), then L2 is unable to reach R2, and $[L2]_{eff}$ is smaller than $[L2]$, leading to a complete lack of cooperativity. If the binding sites R1 and R2 allow for some flexibility in geometry, then we may have a situation as shown in Fig. 4d, where binding of the ligand can be achieved by allowing some mobility in the bound conformation at the cost of suboptimal binding geometry. The cooperativity will not be as great as it would be with ideal geometry and thus the affinity will be stronger, but not by a large amount. This appears to be exactly the situation observed here: affinity is 10× stronger, but CSPs are smaller. Furthermore, single-site mutations have relatively little effect on the affinity or on enzymatic activity, suggesting that the exact shape or complementarity of the binding site is relatively unimportant, consistent with this model.

It is a legitimate question to ask why SH3b should have evolved separate binding sites for G5 and P4, which are located on the protein surface in such a way that simultaneous binding to both sites is not possible. What is the biological advantage? Our data, and the interpretation derived here, provide suggestions. The function of the SH3b domain is to attach lysostaphin to PG, in such a way as to increase access of the catalytic domain to its G5 substrate. It is therefore not desirable for the affinity for PG to be too strong, otherwise SH3b would detach too slowly and not allow the catalytic domain to move from one G5 substrate to another. A good solution is to have two binding sites, both with weak affinity and thus rapid off-rates, and organized so as to provide a moderate degree of cooperativity in binding to the complex substrate. This allows the protein to ‘walk’

around the PG surface, continually keeping at least one site bound, but permitting rapid searching on the PG surface. A very similar solution has been adopted by a number of cellulases, which have two different cellulose-binding domains arranged in tandem^{26–29}.

A comparison of interactions at the two sites with different ligands (Fig. 1) suggests that the larger ligands have weaker interactions at the G5 site, as the G5 interactions (red) decrease more than the P4 interactions (green). This result is at first sight counter-intuitive, because the lysostaphin catalytic domain specifically targets G5. However SH3b should not bind too tightly to G5, because otherwise it would block access of the catalytic domain. It therefore makes sense for the larger (and thus more cell-wall-like) fragments to favor binding of the peptide stem, as long as some specificity for G5 is maintained, and as long as SH3b is not locked into binding at any particular location. We may therefore describe the role of SH3b as to contribute to the initial (weak) binding of the enzyme on the PG surface. This conclusion is also consistent with the observation that the mutations more critical to binding affinity are found in the P4 site, not the G5 site. Surprisingly, and in agreement with this result, the SH3b domain still binds in a dose-dependent manner to the *femAB* PG, which contains crossbridges made of a single glycine residue. This suggests that the recognition of the pentaglycine stem is not essential for the binding of the enzyme with its substrate. On the basis of this result, it is tempting to hypothesize that the catalytic activity of lysostaphin, rather than the binding itself, is the major determinant for the specific hydrolysis of staphylococcal PG. In *Staphylococcus carnosus*, the *femB* mutation is associated with a 3000-fold increase in the minimum inhibitory concentration values for lysostaphin from 0.01 to 32 µg ml⁻¹ (ref. ³⁰). Given the limited impact of the SH3b mutations on binding, this result suggests that the high resistance to lysostaphin in the *femB* mutant is not caused by the slight difference in binding activity of the penta- versus tri-glycine interpeptide bridge, but is mainly due to the decreased enzymatic activity of lysostaphin.

The networks of contacts between the ligand and two sets of SH3 domains strongly suggest that our two-site model for P4–G5 (and therefore true complex sacculus ligand) is physiologically relevant. The observed pocket for the terminal P4 D-Ala is highly complementary in both shape and contact type; a lack of an adjoining pocket for a second D-Ala of a pentapeptide is in keeping with the dominance of tetrapeptides in staphylococcal PG³¹. Residues responsible for P4 recognition are conserved in several homologs present in the Protein Data Bank (PDB) despite the relatively low sequence identity across the entire domain (*S. capitis* ALE-1, PDB accession 1R77, 83% sequence identity¹⁹; *Staphylococcus* phage GH15 lysis, PDB accession 2MK5, 49% sequence identity³²; and phage phi7917 lysis, PDB accession 5D76, 30% sequence identity, unpublished). These related structures have features that validate our identification of the P4-binding site (Supplementary Fig. 4): in ALE-1 a purification tag places a lysine in an identical position to the K3 crosslink, and in phi7917 a muramyl dipeptide cleavage product has bound in this region. Our identification of a ‘second’ binding site supplementing the ‘traditional’ pentaglycine cleft may have implications for other SH3b and SH3-like domains that are used in varying architectures to recognize PG in organisms that do not utilize the G5 crossbridge.

No major difference exists between the structure of the SH3b domain in its apo form (PDB accession 4LXC) and in complex with the P4–G5 ligand (this work), suggesting that the ligand displays a dynamic structure to ‘fit’ within the binding clefts present on the SH3b domain. Previous NMR studies support this idea and have shown that the D-Lac, L-Ala and D-Glu adopt a limited number of conformers, whereas the L-Lys–D-Ala termini are disordered (with no nuclear Overhauser effects contacts observed³³). Further relaxation measurements using the P4–G5 ligand could be carried out to test this hypothesis, but it appears difficult to extrapolate relaxation experiments to a complex molecule such as PG.

The data presented here provide an explanation as to why the binding activity of the SH3b domain of lysostaphin is not affected by exogenous pentaglycine or its own catalytic products²¹; our model suggests that the muropeptide interactions are only satisfied when presented by non-contiguous epitopes of mature physiological PG. The location of these sites on different faces of the SH3b molecule ensures that both are unlikely to be contacted by a soluble, torsionally less-restricted, fragment. We hypothesize that this will be an excellent method for processive degradation of the PG.

The structure of the SH3b domain in complex with the P4–G5 peptide sheds light on previously published NMR analyses³⁴ and those described in this manuscript, revealing the existence of two independent binding sites on opposite sides of the SH3b domain. The binding mechanism described here is consistent with the formation of large protein aggregates during titration with complex PG fragments. Recognition of the same PG peptide stem by independent SH3b domains (referred to as ‘clustering’) leads to an effective increase in enzyme concentration at the cell surface. In agreement with this hypothesis, the direct observation of *S. aureus* cell wall digestion by lysostaphin using atomic force microscopy revealed the existence of nanoscale perforations that precede cell lysis³⁵.

Online content

Any methods, additional references, Nature Research reporting summaries, source data, statements of code and data availability and associated accession codes are available at <https://doi.org/10.1038/s41589-019-0393-4>.

Received: 11 June 2018; Accepted: 21 September 2019;

Published online: 04 November 2019

References

1. Schindler, C. A. & Schuhardt, V. T. Lysostaphin: a new bacteriolytic agent for the *Staphylococcus*. *Proc. Natl Acad. Sci. USA* **51**, 414–421 (1964).
2. Schindler, C. A. & Schuhardt, V. T. Purification and properties of Lysostaphin—a lytic agent for *Staphylococcus aureus*. *Biochim. Biophys. Acta* **97**, 242–250 (1965).
3. Thumm, G. & Götz, F. Studies on prolysostaphin processing and characterization of the lysostaphin immunity factor (Lif) of *Staphylococcus simulans* biovar *staphylolyticus*. *Mol. Microbiol* **23**, 1251–1265 (1997).
4. Wu, J. A., Kusuma, C., Mond, J. J. & Kokai-Kun, J. F. Lysostaphin disrupts *Staphylococcus aureus* and *Staphylococcus epidermidis* biofilms on artificial surfaces. *Antimicrob. Agents Chemother.* **47**, 3407–3414 (2003).
5. Climo, M. W., Patron, R. L., Goldstein, B. P. & Archer, G. L. Lysostaphin treatment of experimental methicillin-resistant *Staphylococcus aureus* aortic valve endocarditis. *Antimicrob. Agents Chemother.* **42**, 1355–1360 (1998).
6. Dajcs, J. J. et al. Lysostaphin treatment of methicillin-resistant *Staphylococcus aureus* keratitis in the rabbit. *Invest Ophthalmol. Vis. Sci.* **41**, 1432–1437 (2000).
7. Johnson, C. T. et al. Hydrogel delivery of lysostaphin eliminates orthopedic implant infection by *Staphylococcus aureus* and supports fracture healing. *Proc. Natl Acad. Sci. USA* **115**, E4960–E4969 (2018).
8. Kiri, N., Archer, G. & Climo, M. W. Combinations of lysostaphin with β-lactams are synergistic against oxacillin-resistant *Staphylococcus epidermidis*. *Antimicrob. Agents Chemother.* **46**, 2017–2020 (2002).
9. Kokai-Kun, J. F., Chanturiya, T. & Mond, J. J. Lysostaphin as a treatment for systemic *Staphylococcus aureus* infection in a mouse model. *J. Antimicrob. Chemother.* **60**, 1051–1059 (2007).
10. Kokai-Kun, J. F., Walsh, S. M., Chanturiya, T. & Mond, J. J. Lysostaphin cream eradicates *Staphylococcus aureus* nasal colonization in a cotton rat model. *Antimicrob. Agents Chemother.* **47**, 1589–1597 (2003).
11. Satishkumar, R. et al. Evaluation of the antimicrobial activity of lysostaphin-coated hernia repair meshes. *Antimicrob. Agents Chemother.* **55**, 4379–4385 (2011).
12. Blazanovic, K. et al. Structure-based redesign of lysostaphin yields potent antistaphylococcal enzymes that evade immune cell surveillance. *Mol. Ther. Methods Clin. Dev.* **2**, 15021 (2015).
13. Zhao, H. et al. Depletion of T cell epitopes in lysostaphin mitigates anti-drug antibody response and enhances antibacterial efficacy in vivo. *Chem. Biol.* **22**, 629–639 (2015).
14. Liu, Y. et al. Immunomimetic designer cells protect mice from MRSA infection. *Cell* **174**, 259–270 (2018).

15. Raz, A., Serrano, A., Thaker, M., Alston, T. & Fischetti, V. A. Lysostaphin lysisbody leads to effective opsonization and killing of methicillin-resistant *Staphylococcus aureus* in a murine model. *Antimicrob. Agents Chemother.* **62**, e01056-18 (2018).
16. Wall, R. J. et al. Genetically enhanced cows resist intramammary *Staphylococcus aureus* infection. *Nat. Biotechnol.* **23**, 445–451 (2005).
17. Wittekind, M. & Schuch, R. Cell wall hydrolases and antibiotics: exploiting synergy to create efficacious new antimicrobial treatments. *Curr. Opin. Microbiol.* **33**, 18–24 (2016).
18. Baba, T. & Schneewind, O. Target cell specificity of a bacteriocin molecule: a C-terminal signal directs lysostaphin to the cell wall of *Staphylococcus aureus*. *EMBO J.* **15**, 4789–4797 (1996).
19. Lu, J. Z., Fujiwara, T., Komatsuza, H., Sugai, M. & Sakon, J. Cell wall-targeting domain of glycylglycine endopeptidase distinguishes among peptidoglycan cross-bridges. *J. Biol. Chem.* **281**, 549–558 (2006).
20. Mitkowski, P. et al. Structural bases of peptidoglycan recognition by lysostaphin SH3b domain. *Sci. Rep.* **9**, 5965 (2019).
21. Gründling, A. & Schneewind, O. Cross-linked peptidoglycan mediates lysostaphin binding to the cell wall envelope of *Staphylococcus aureus*. *J. Bacteriol.* **188**, 2463–2472 (2006).
22. Tamai, E. et al. X-ray structure of a novel endolysin encoded by episomal phage phiSM101 of *Clostridium perfringens*. *Mol. Microbiol.* **92**, 326–337 (2014).
23. Shaner, N. C. et al. A bright monomeric green fluorescent protein derived from *Branchiostoma lanceolatum*. *Nat. Methods* **10**, 407–409 (2013).
24. Williamson, M. P *How Proteins Work*. (Garland Science, 2011). .
25. Zhou, H. X. Quantitative relation between intermolecular and intramolecular binding of pro-rich peptides to SH3 domains. *Biophys. J.* **91**, 3170–3181 (2006).
26. Bolam, D. N. et al. *Pseudomonas* cellulose-binding domains mediate their effects by increasing enzyme substrate proximity. *Biochem. J.* **331**, 775–781 (1998).
27. Gill, J. et al. The type II and X cellulose-binding domains of *Pseudomonas* xylanase A potentiate catalytic activity against complex substrates by a common mechanism. *Biochem. J.* **342**, 473–480 (1999).
28. Nagy, T. et al. Characterization of a double dockerin from the cellulosome of the anaerobic fungus *Piromyces equi*. *J. Mol. Biol.* **373**, 612–622 (2007).
29. Raghothama, S. et al. Characterization of a cellulosome dockerin domain from the anaerobic fungus *Piromyces equi*. *Nat. Struct. Biol.* **8**, 775–778 (2001).
30. Nega, M. et al. Secretome analysis revealed adaptive and non-adaptive responses of the *Staphylococcus carnosus* *femB* mutant. *Proteomics* **15**, 1268–1279 (2015).
31. Gally, D. & Archibald, A. R. Cell wall assembly in *Staphylococcus aureus*: proposed absence of secondary crosslinking reactions. *J. Gen. Microbiol.* **139**, 1907–1913 (1993).
32. Gu, J. et al. Structural and biochemical characterization reveals LysGH15 as an unprecedented “EF-hand-like” calcium-binding phage lyssin. *PLoS Pathog.* **10**, e1004109 (2014).
33. Meroueh, S. O. et al. Three-dimensional structure of the bacterial cell wall peptidoglycan. *Proc. Natl Acad. Sci. USA* **103**, 4404–4409 (2006).
34. Tossavainen, H. et al. Structural and functional insights into lysostaphin–substrate interaction. *Front. Mol. Biosci.* **5**, 60 (2018).
35. Francius, G., Domenech, O., Mingeot-Leclercq, M. P. & Dufrêne, Y. F. Direct observation of *Staphylococcus aureus* cell wall digestion by lysostaphin. *J. Bacteriol.* **190**, 7904–7909 (2008).

Acknowledgements

L.S.G.-D. is a PhD student funded by the Mexican government through a CONACYT scholarship. H.W.-M. is supported by a BBSRC MIBTP studentship. We thank the BBSRC and EPSRC for funding to upgrade the 600- and 800-MHz spectrometers, respectively (grant numbers BB/R000727/1 and EP/S01358X/1). The work in the laboratory of I.S. is supported by the Foundation for Polish Science (FNP) program, co-financed by the European Union under the European Regional Development Fund (grant TEAMTECH/2016-3/19).

Author contributions

S.M. conceived the project and designed experiments with M.P.W. and A.L.L. A.M.H. and A.J.R. assigned the SH3b spectrum. L.S.G.-D. carried out all NMR experiments and analyzed them with the help of A.M.H. and M.P.W. B.S. and L.S.G.-D. built all SH3b recombinant proteins to carry out functional assays and crystallographic analyses. A.W.-M. crystallized the protein and solved the structure with the help of A.L.L. E.J. and I.S. provided reagents. L.S.G.-D., H.W.-M., B.S., A.M.H., M.P.W., A.L.L. and S.M. analyzed the data. L.S.G.-D., S.M., A.L.L. and M.P.W. wrote the manuscript.

Competing interests

The authors declare no competing interests.

Additional information

Supplementary information is available for this paper at <https://doi.org/10.1038/s41589-019-0393-4>.

Correspondence and requests for materials should be addressed to M.P.W., A.L.L. or S.M.

Reprints and permissions information is available at www.nature.com/reprints.

Publisher's note Springer Nature remains neutral with regard to jurisdictional claims in published maps and institutional affiliations.

© The Author(s), under exclusive licence to Springer Nature America, Inc. 2019

Methods

Bacterial strains, plasmids and growth conditions. Bacterial strains and plasmids used in this study are described in Supplementary Table 3. *E. coli* Lemo21 (DE3) and NEB5 α strains were grown at 37°C in LB or M9 minimal medium containing 1 g l⁻¹ of ¹⁵NH₄Cl (and 2 g l⁻¹ ¹³C₆-glucose where necessary) and supplemented with ampicillin at a concentration of 100 µg ml⁻¹.

Construction of recombinant plasmids for protein production. Both plasmids expressing full-length lysostaphin (pET-Lss) and the SH3b domains with a non-cleavable N-terminal His-tag for NMR studies (pET-SH3b) have been previously described^{36,37}. The plasmid encoding the SH3b-mNeonGreen fusion (pET-SH3b-NG) was constructed by Gibson assembly using a DNA synthetic fragment (Integrated DNA Technology) cloned into the vector pET2818 cut with NcoI and BamHI. Plasmid pET-SH3b-TEV used to produce the SH3b domain without a tag for X-ray crystallography was constructed by Gibson assembly using a synthetic DNA fragment (Integrated DNA Technology) cloned into pET2817 digested with NcoI and BamHI. The amino acid sequences of the wild-type recombinant proteins are described in Supplementary Fig. 8.

Site-directed mutagenesis. Mutagenesis of plasmids pET-SH3b and pET-Lss was performed using the GeneArt site-directed mutagenesis system (Thermo Fisher Scientific). All primers used in this study are described in the Supplementary Table 4. The same pair of oligonucleotides was used to introduce mutations in both plasmids, except for the N405A and W489L substitutions, which required distinct pairs of oligonucleotides to build mNeonGreen fusions and lysostaphin mutants.

Purification of recombinant lysostaphin and lysostaphin SH3b domains. Cells were grown to an optical density at 600 nm (OD₆₀₀) of 0.7 in LB or M9 medium for NMR analyses and protein production was induced by the addition of 1 mM IPTG. After 4 h, induced cells were collected and resuspended in buffer A (50 mM Tris-HCl, 500 mM NaCl, pH 8.0) and crude lysates were obtained by sonication (3 × 30 s, 20% output; Bransonic Sonifier 450). Soluble proteins were loaded onto a HiTrap IMAC column (GE Healthcare) charged with Ni²⁺ or Zn²⁺ ions for SH3b (alone or fused to mNeonGreen) or full-length lysostaphin, respectively. His-tagged proteins were eluted with a 20-column-volume linear gradient of buffer B (500 mM imidazole, 50 mM Tris-HCl, 500 mM NaCl, pH 8.0). Recombinant His-tagged proteins were concentrated and purified by size-exclusion chromatography on a Superdex 75 HR column (GE Healthcare). For NMR experiments, proteins were purified using 50 mM Na₂HPO₄ (pH 6.0). All purified proteins were analyzed by SDS-PAGE.

For crystallography experiments, the SH3b domain was produced using plasmid pET-SH3b-TEV. The N-terminal tag was removed using recombinant TEV protease (0.5 mg of TEV per mg of SH3b protein). Digestions were performed at 37°C overnight in buffer C (150 mM NaCl, 50 mM Tris-HCl, pH 8.35). Following digestion, proteins were loaded onto a HiTrap IMAC column, and cleaved SH3b proteins were recovered in the flow through. Protein concentrations were determined using absorbance at 280 nm.

The characterization of all recombinant proteins is described in the supplementary information (Supplementary Figs. 8–12).

Purification of *S. aureus* PG sacculi. PG sacculi were isolated from exponentially growing *S. aureus* cells as previously described³⁸. Pure PG was freeze-dried and resuspended at a final concentration of 25 mg ml⁻¹.

PG digestions for NMR titration assays. *S. aureus* PG was digested with mutanolysin (Sigma). To purify PG dimers (GM-P5-G5-GM-P4-G5), 180 mg of PG were digested with 2.5 mg of mutanolysin in a final volume of 5 ml using 20 mM phosphate buffer (pH 6.0). After overnight incubation, the enzyme was heat inactivated. Half of the sample was used to purify dimers. The pH of the other half of digestion was adjusted to 7.5 and it was further digested with 2 mg of EnpA to generate disaccharide-peptides. EnpA was heat inactivated.

Purification of PG fragments by reverse-phase HPLC. Before reverse-phase HPLC analysis and fractionation, soluble PG fragments were reduced with sodium borohydride to eliminate double peaks corresponding to the α - and β -anomers as previously described³⁸. Fractionation of material corresponding to the digestion of 50 mg of PG was carried out on a Hypersil GOLD aQ column (C18; 21 × 250 mm; Thermo Scientific Fisher) and separated at a flow rate of 10 ml min⁻¹ using 10 mM ammonium phosphate, pH 5.5 as a mobile phase (buffer A). After a short isocratic step (two column volumes), PG fragments were eluted with a 15-column-volume methanol linear gradient (0–30%) in buffer A. Individual peaks were collected, freeze-dried and analyzed by mass spectrometry. The fractions corresponding to the major dimer (GM-P5-G5-GM-P4-G5) were desalted by HPLC using a water-acetonitrile gradient, freeze-dried and resuspended in MilliQ water.

Production of PG fragments by chemical synthesis. The tetrasaccharide (GMGM) was described previously³⁹. All peptides and branched peptides

(>95% purity) were purchased from Peptide Protein Research. Purity was assessed by HPLC and mass spectrometry. The characterization of all ligands is described in the supplementary information. The pentaglycine peptide was purchased from Sigma Aldrich (cat. no. G5755).

Crystallography and structure determination. Crystallization was initiated via standard screening in sitting drop 96-well clover-leaf crystallography trays at 18 mg ml⁻¹ with 3.41 mM AyQK[GGGGG]A in a 1:2 drop ratio of screening agent to protein solution. The trays were incubated at 18°C. Tetragonal bipyramidal crystals formed within the first 48 h in 100 mM Bis-Tris, pH 5.5, 25% (wt/vol) poly(ethylene) glycol 3350 and 200 mM ammonium sulphate.

Crystals were cryo-protected using the above conditions (including AyQK[GGGGG]A to maintain the ligand–protein complex) and additional 20% (vol/vol) ethylene glycol. Two datasets were collected (Supplementary Table 5): a high-resolution set at the I03 beamline, Diamond Light Source, Oxford and a second set on a Rigaku Micromax home source. Data were processed with XiaII/XDS⁴⁰. The *B* factors for the high-resolution set were higher than expected, but match that of the Wilson *B*, and the dataset has a normal intensity distribution. An initial model was solved using the existing apo structure 5LEO (ref. ²⁰) as a molecular replacement model in PHASER⁴¹, and the corresponding structure was autobuilt using PHENIX⁴², with the ligand added via visual inspection of the difference map. The structure was updated and refined using COOT⁴³, PHENIX⁴² and PDB-redo⁴⁴, resulting in a final structure with an *R/R_{free}* of 19.9%/23.0%.

NMR experiments. NMR experiments were conducted on Bruker Avance I 800 and DRX-600 spectrometers at 298 K. Two-dimensional NHSQC experiments were carried out using the b_hsqcetf3gpsi pulse program (Bruker) with a relaxation delay of 1 s, 128 complex increments (approximately 1 h 18 m per spectrum). Lysostaphin SH3b proteins were quantified by measuring the absorbance at 280 nm and adjusted to a concentration of 60 µM in 50 mM Na₂HPO₄, pH 6.0. All ligands were quantified by NMR on the basis of the intensity of methyl protons using trimethylsilylpropanoic acid (TSP) as a standard. ¹⁵N HSQC experiments and CSP analyses were performed as previously described³⁹.

PG binding assays. The PG binding activity of SH3b domains was studied using in-gel fluorescence. Protein amounts equivalent to 3 µg of the wild-type recombinant SH3b-mNeonGreen were adjusted on the basis of fluorescence intensity of the bands corresponding to the full-length proteins. Following incubation in the presence of increasing amounts of PG (0–400 µg) in a final volume of 40 µl for 20 min at room temperature, PG and bound proteins were pelleted at 17,000g for 5 min. Twenty microliters of supernatant corresponding to unbound proteins were loaded on an SDS-PAGE gel and scanned using a BioRad Chemidoc XRS⁺ system. Fluorescence intensity was quantified using the ImageJ software. The percentage of binding was determined using the signal intensity measured in the absence of PG as a reference.

Lysostaphin activity assays. *S. aureus* SH1000 (ref. ⁴⁵) was grown to an optical density OD₆₀₀ of 1.0. Cells were collected, resuspended in distilled water, autoclaved and incorporated in agar plates at a final OD₆₀₀ of 0.5. Five microliters corresponding to serial dilutions of the recombinant lysostaphin proteins were spotted on the plates containing autoclaved cells as a substrate and incubated overnight at 37°C. Lytic activities were detected as clearing zones and compared by determining the lowest amount of enzyme giving a detectable digestion of the substrate.

Reporting Summary. Further information on research design is available in the Nature Research Reporting Summary linked to this article.

Data availability

Structural data have been deposited in the PDB with coordinate accession numbers 6RK4 (high-resolution set) and 6RJE (home source set). All other data generated or analyzed during this study are included in this article and its supplementary information or are available from the corresponding authors upon request.

References

36. Jagielska, E., Chojnacka, O. & Sabala, I. LytM fusion with SH3b-like domain expands its activity to physiological conditions. *Micro. Drug Resist.* **22**, 461–469 (2016).
37. Sabala, I. et al. Crystal structure of the antimicrobial peptidase lysostaphin from *Staphylococcus simulans*. *FEBS J.* **281**, 4112–4122 (2014).
38. Mesnage, S., Chau, F., Dubost, L. & Arthur, M. Role of *N*-acetylglucosaminidase and *N*-acetylmuramidase activities in *Enterococcus faecalis* peptidoglycan metabolism. *J. Biol. Chem.* **283**, 19845–19853 (2008).
39. Mesnage, S. et al. Molecular basis for bacterial peptidoglycan recognition by LysM domains. *Nat. Commun.* **5**, 4269 (2014).
40. Kabsch, W. XDS. *Acta Crystallogr. D Biol. Crystallogr.* **66**, 125–132 (2010).

41. McCoy, A. J. et al. Phaser crystallographic software. *J. Appl Crystallogr.* **40**, 658–674 (2007).
42. Zwart, P. H. et al. Automated structure solution with the PHENIX suite. *Methods Mol. Biol.* **426**, 419–435 (2008).
43. Emsley, P. & Cowtan, K. Coot: model-building tools for molecular graphics. *Acta Crystallogr. D Biol. Crystallogr.* **60**, 2126–2132 (2004).
44. Joosten, R. P., Joosten, K., Cohen, S. X., Vriend, G. & Perrakis, A. Automatic rebuilding and optimization of crystallographic structures in the Protein Data Bank. *Bioinformatics* **27**, 3392–3398 (2011).
45. Horsburgh, M. J. et al. σ^B modulates virulence determinant expression and stress resistance: characterization of a functional rsbU strain derived from *Staphylococcus aureus* 8325-4. *J. Bacteriol.* **184**, 5457–5467 (2002).

Reporting Summary

Nature Research wishes to improve the reproducibility of the work that we publish. This form provides structure for consistency and transparency in reporting. For further information on Nature Research policies, see [Authors & Referees](#) and the [Editorial Policy Checklist](#).

Statistics

For all statistical analyses, confirm that the following items are present in the figure legend, table legend, main text, or Methods section.

n/a Confirmed

- The exact sample size (n) for each experimental group/condition, given as a discrete number and unit of measurement
- A statement on whether measurements were taken from distinct samples or whether the same sample was measured repeatedly
- The statistical test(s) used AND whether they are one- or two-sided
Only common tests should be described solely by name; describe more complex techniques in the Methods section.
- A description of all covariates tested
- A description of any assumptions or corrections, such as tests of normality and adjustment for multiple comparisons
- A full description of the statistical parameters including central tendency (e.g. means) or other basic estimates (e.g. regression coefficient) AND variation (e.g. standard deviation) or associated estimates of uncertainty (e.g. confidence intervals)
- For null hypothesis testing, the test statistic (e.g. F , t , r) with confidence intervals, effect sizes, degrees of freedom and P value noted
Give P values as exact values whenever suitable.
- For Bayesian analysis, information on the choice of priors and Markov chain Monte Carlo settings
- For hierarchical and complex designs, identification of the appropriate level for tests and full reporting of outcomes
- Estimates of effect sizes (e.g. Cohen's d , Pearson's r), indicating how they were calculated

Our web collection on [statistics for biologists](#) contains articles on many of the points above.

Software and code

Policy information about [availability of computer code](#)

Data collection

Beamline software used as appropriate.

Data analysis

CCP4 and Phenix suites used to process crystallographic data. NMR spectra were processed and analysed using TOPSPIN (versions 1.3 and 2.1) and FELIX 2007 software (Felix NMR, Inc., San Diego, CA).

For manuscripts utilizing custom algorithms or software that are central to the research but not yet described in published literature, software must be made available to editors/reviewers. We strongly encourage code deposition in a community repository (e.g. GitHub). See the Nature Research [guidelines for submitting code & software](#) for further information.

Data

Policy information about [availability of data](#)

All manuscripts must include a [data availability statement](#). This statement should provide the following information, where applicable:

- Accession codes, unique identifiers, or web links for publicly available datasets
- A list of figures that have associated raw data
- A description of any restrictions on data availability

Co-ordinates and structure factors have been deposited in the RCSB with accession codes 6RK4 (high-resolution set) and 6RJE (home source set). Other data are available from the corresponding author upon reasonable request.

Field-specific reporting

Please select the one below that is the best fit for your research. If you are not sure, read the appropriate sections before making your selection.

Life sciences study design

All studies must disclose on these points even when the disclosure is negative.

| | |
|-----------------|--|
| Sample size | Owing to nature of our investigations, there was no need for this to be performed. |
| Data exclusions | No data were excluded from the analyses. |
| Replication | Replicates clearly stated in text where appropriate. |
| Randomization | Not applicable |
| Blinding | Not applicable |

Reporting for specific materials, systems and methods

We require information from authors about some types of materials, experimental systems and methods used in many studies. Here, indicate whether each material, system or method listed is relevant to your study. If you are not sure if a list item applies to your research, read the appropriate section before selecting a response.

| Materials & experimental systems | | Methods | |
|-------------------------------------|-----------------------------|-------------------------------------|------------------------|
| n/a | Involved in the study | n/a | Involved in the study |
| <input checked="" type="checkbox"/> | Antibodies | <input checked="" type="checkbox"/> | ChIP-seq |
| <input checked="" type="checkbox"/> | Eukaryotic cell lines | <input checked="" type="checkbox"/> | Flow cytometry |
| <input checked="" type="checkbox"/> | Palaeontology | <input checked="" type="checkbox"/> | MRI-based neuroimaging |
| <input checked="" type="checkbox"/> | Animals and other organisms | | |
| <input checked="" type="checkbox"/> | Human research participants | | |
| <input checked="" type="checkbox"/> | Clinical data | | |